Electronic Supplementary Material (ESI) for Molecular Systems Design & Engineering.

Supporting Information

Probing Transport Limitations in Thick Sintered Battery Electrodes with Neutron Imaging

Ziyang Nie,[a] Samuel Ong,[a] Daniel S. Hussey,[b] Jacob M. LaManna,[b] David L. Jacobson,[b] Gary M. Koenig Jr.*[a]

[a] Department of Chemical Engineering, University of Virginia, 102 Engineers Way, Charlottesville, VA, USA 22904-4741

[b] National Institute of Standards and Technology Physical Measurements Laboratory, Gaithersburg, MD, USA 20899-8461

Email: gary.koenig@virginia.edu

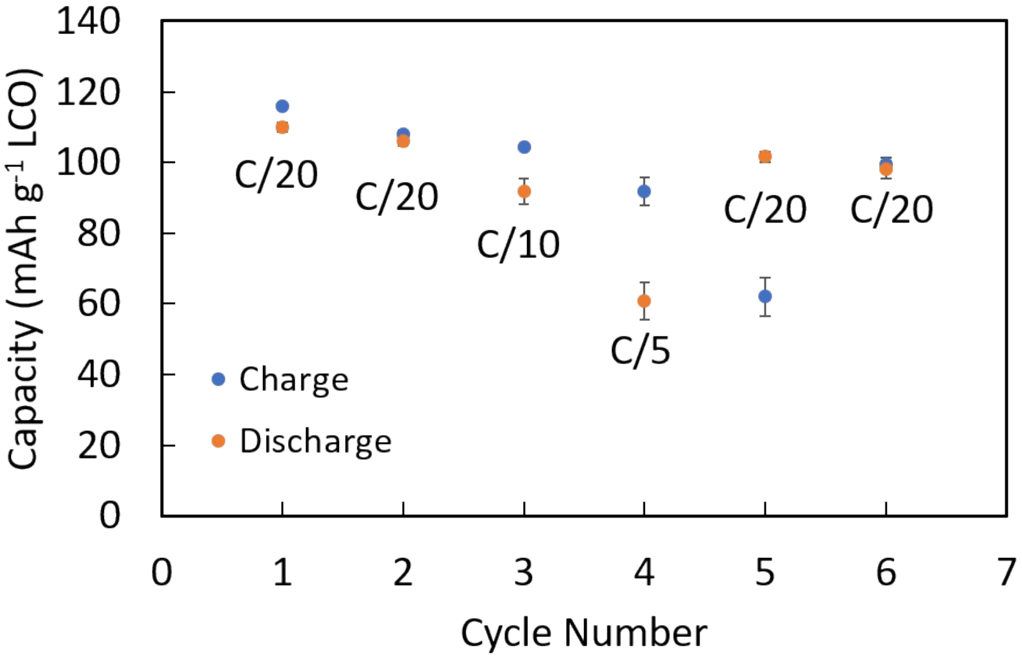

Fig. S1. Average electrochemical charge (blue circles) and discharge (orange circles) capacities for three nominally identical sintered LTO/LCO coin cells which were processed the same as the cell used in the neutron imaging experiment. Error bars represent the standard deviations for the three cells, and where error bars are not apparent they were smaller than the data markers. The charge rate for all cycles was C/20 (7.5 mA g^{-1} LCO) while the discharge rates were C/20 (cycles 1, 2, 5, and 6), C/10 (cycle 3, 15.0 mA g^{-1} LCO), and C/5 (cycle 4, 30 mA g^{-1} LCO), with the discharge rate labelled on the figure.

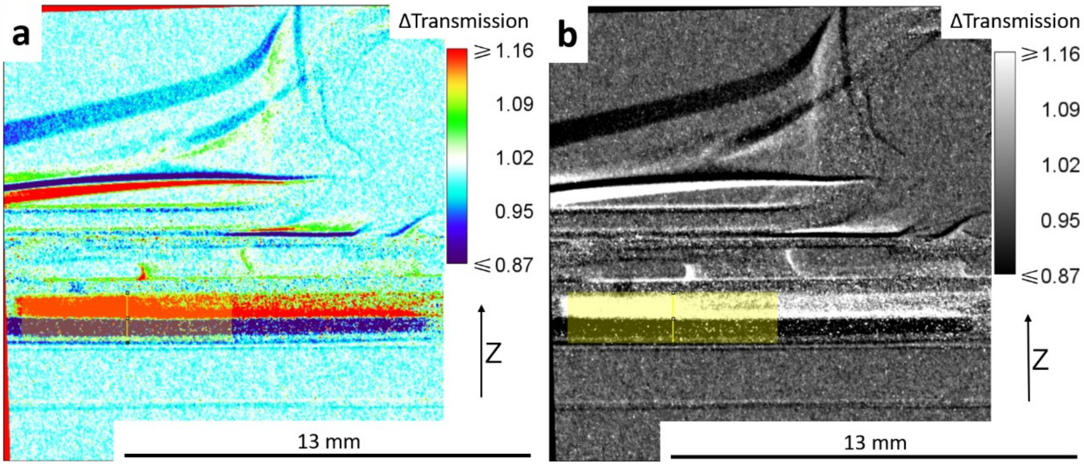

Fig. S2. Example color scale (a) and grey scale (b) of the same neutron images from the end of the first discharge (images are from D^{1}_{832} in Fig. 2 in the main text). The yellow shaded region in the images represent the area chosen for line scans to obtain the average transmission profiles as a function of depth in the cell (z-direction as shown in (a) and (b)). The grey scale image is given here to more clearly show the yellow line scan region.

Tortuosity measurement of sintered electrode

The tortuosity measurement was based on the publication of Thorat *et al.*[1] For tortuosity analysis, only LTO pellets were evaluated. The electronic conductivity of the LCO is much greater than the LTO and results in incorrectly low measured resistance in the cell, consistent with other reports in the literature.[2,3] As described in the main text, although LTO electronic conductivity has been reported to be much lower than LCO, the neutron radiographs and polarization curves presented in this study suggested that the LTO electronic conductivity was likely greater than expected. Thus, measured values of tortuosity described below should be considered as lower bounds for the actual tortuosity and Bruggeman exponent for the electrodes. However, the electrodes were prepared identically and thus the relative comparison between coin cell and split cell measurements described below should still be appropriate. The LTO and LCO have similar particle sizes and particle size distributions which should result in similar tortuosity in the resulting pellets. A Li/Li symmetric cell was constructed as illustrated in Fig S3. This structure was assembled both by crimping within a CR2032 coin cell as well by fastening together a split cell (MTI corporation). Previous experience in assembling coin cells has sometimes resulted in cracking in the porous thin films, while in the split cell the compression is much more gradual. All pellets used in the split cell were extracted after electrochemical evaluation and confirmed not to have cracks. The LTO within coin cells required excessive physical force to harvest the electrodes and thus it could not be assessed if cracking was due to the initial crimping or the pellet extraction process.

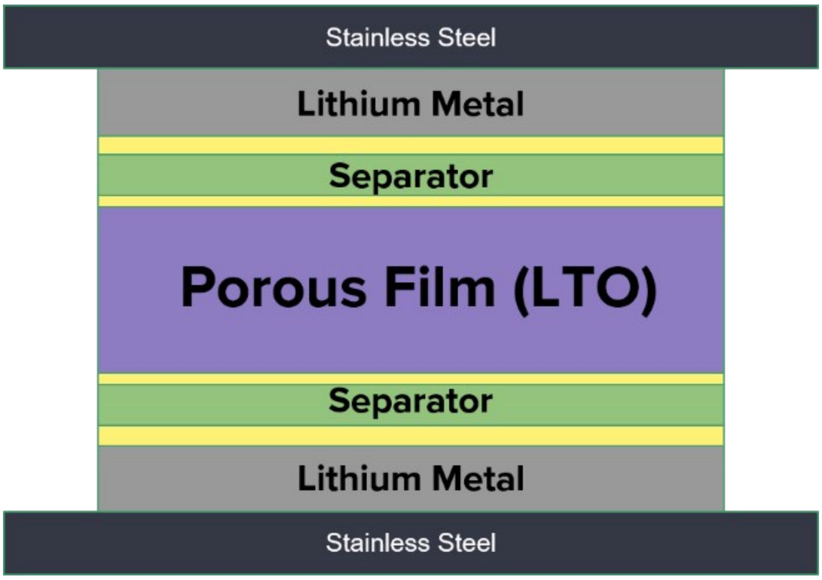

Fig. S3. Illustration of a cross-sectional view of the Li/Li symmetric cell used for tortuosity measurements.

Both the coin cell and the split cell were evaluated using potentiostatic electrochemical impedance spectroscopy (EIS). From the EIS results, the high frequency intercept (R_∞) was extracted (Fig. S4). The tortuosity (τ) and Bruggeman exponent (α) were calculated using the following equations:

$$k_{eff} = \frac{L}{A \times R_\infty}$$

$$\tau = \frac{k_{real} \times \epsilon}{k_{eff}}$$

$$\tau = \epsilon^{1 - \alpha}$$

where L is the thickness of the porous film; A is its cross-sectional area; k_{eff} is the effective ionic conductivity of the electrolyte; ϵ is the porosity; k_{real} is the intrinsic conductivity of the electrolyte with a value of 5.41 mS/cm (measured using a conductivity probe).

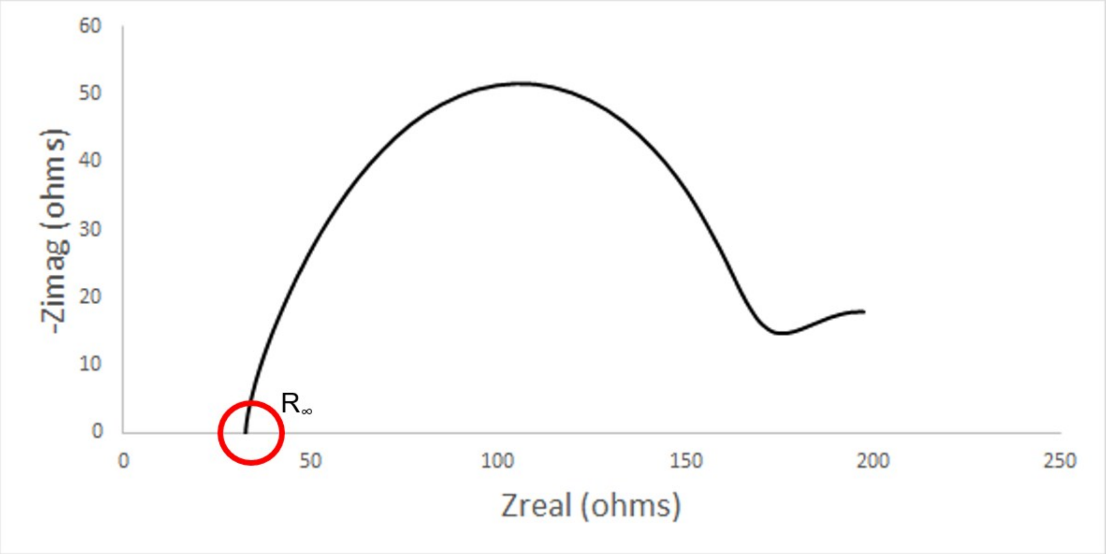

Fig. S4. Example of EIS results form a Li/Li symmetric cell as shown in Fig. S3 and R_∞

The results of multiple samples with different cell structures are shown in Table S1. From the average results, the split cell with an uncracked pellet showed good agreement with the commonly assumed empirical Bruggeman exponent value (α=1.5). The coin cell samples all showed a value less than 1.5, which indicated some cracking likely occurred during the crimping process.

Table S1. Bruggeman exponent for different Li/Li symmetric cell

	Bruggeman Exponent	
Sample No.	Coin Cell	Split Cell
1	1.28	1.49

2	1.38	1.58
3	1.18	1.39
4	1.10	1.49
5		1.43
Average	1.23	1.48

Additional Details on Electrolyte Properties

As mentioned above the measured ionic conductivity of the bulk electrolyte as prepared was of 5.41 mS/cm, however, for the detailed calculations done in this study additional electrolyte properties were required beyond this single conductivity value and the bulk salt concentration of 1.2 mol/L $LiPF_6$.

The electrolyte properties as a function of concentration used in calculations were originally from Newman's Dualfoil code.[4] These properties, acknowledged in the code, were measured by Capiglia *et al*[5] and Doyle[6] and are listed below:

Diffusion coefficient:

$$D = 5.34 \times 10^{-10} \times \varepsilon^{\alpha} e^{6.5 \times 10^{-4} c}$$

Transference number:
$t^{+} = 0.4$

Conductivity:
$\kappa = \varepsilon^{\alpha}(0.0911 + 1.9101 \times 10^{-3} c - 1.052 \times 10^{-6} c^{2} + 1.554 \times 10^{-10} c^{3})$

List of symbols:

c	Concentration of electrolyte (mol/m^3)
D	Diffusion coefficient (m^2/s)
t^+	Transference number
α	Bruggeman exponent
ε	Porosity
κ	Conductivity of electrolyte (S/m)

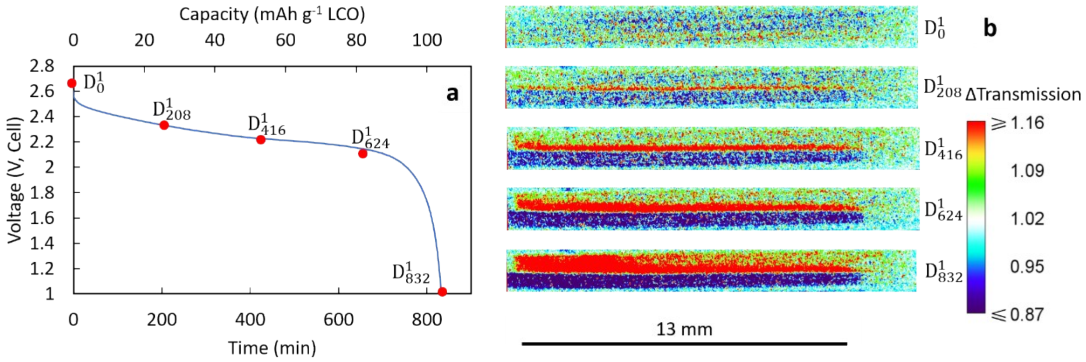

Fig. S5. (a) Discharge profiles of D^1 at C/20. (b) Neutron images corresponding to the time points noted in (a).

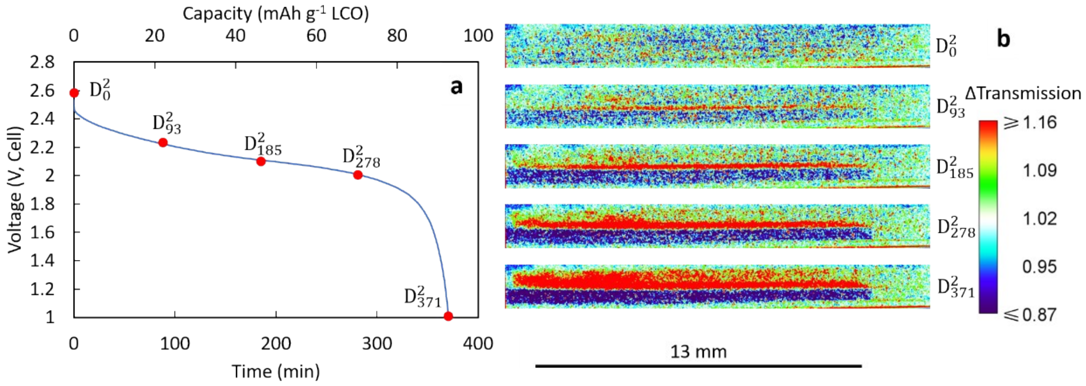

Fig. S6. (a) Discharge profiles of D^2 at C/10. (b) Neutron images corresponding to the time points noted in (a).

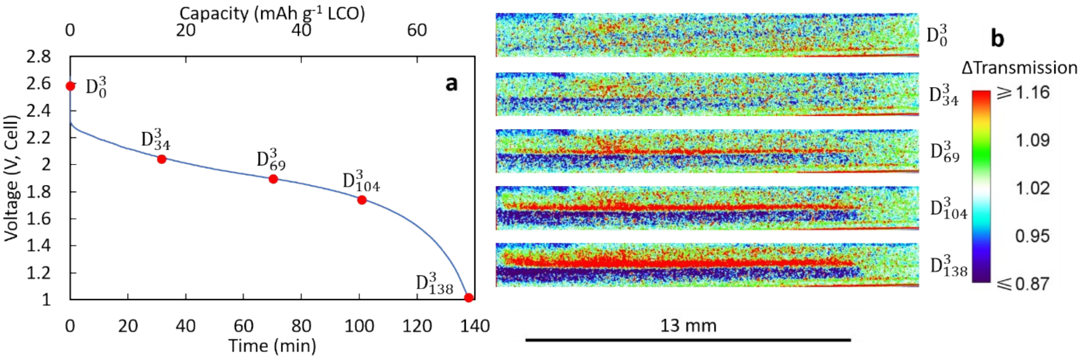

Fig. S7. (a) Discharge profiles of D^3 at C/5. (b) Neutron images corresponding to the time points noted in (a).

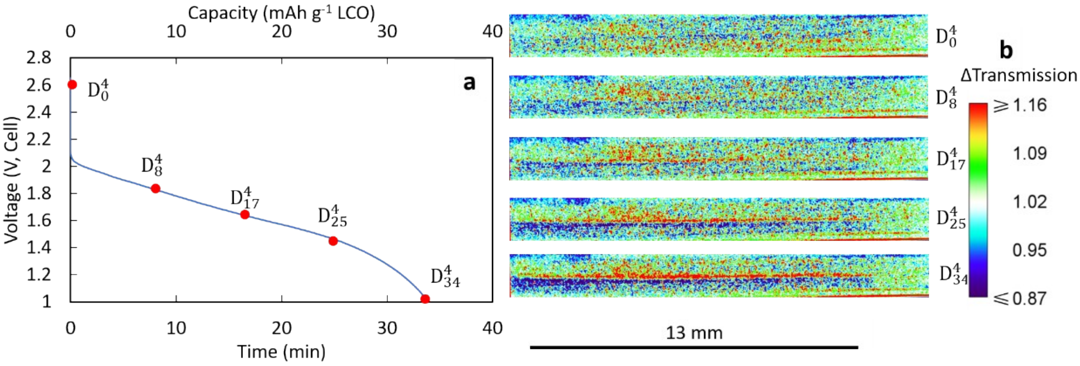

Fig. S8. (a) Discharge profiles of D^4 at C/2.5. (b) Neutron images corresponding to the time points noted in (a).

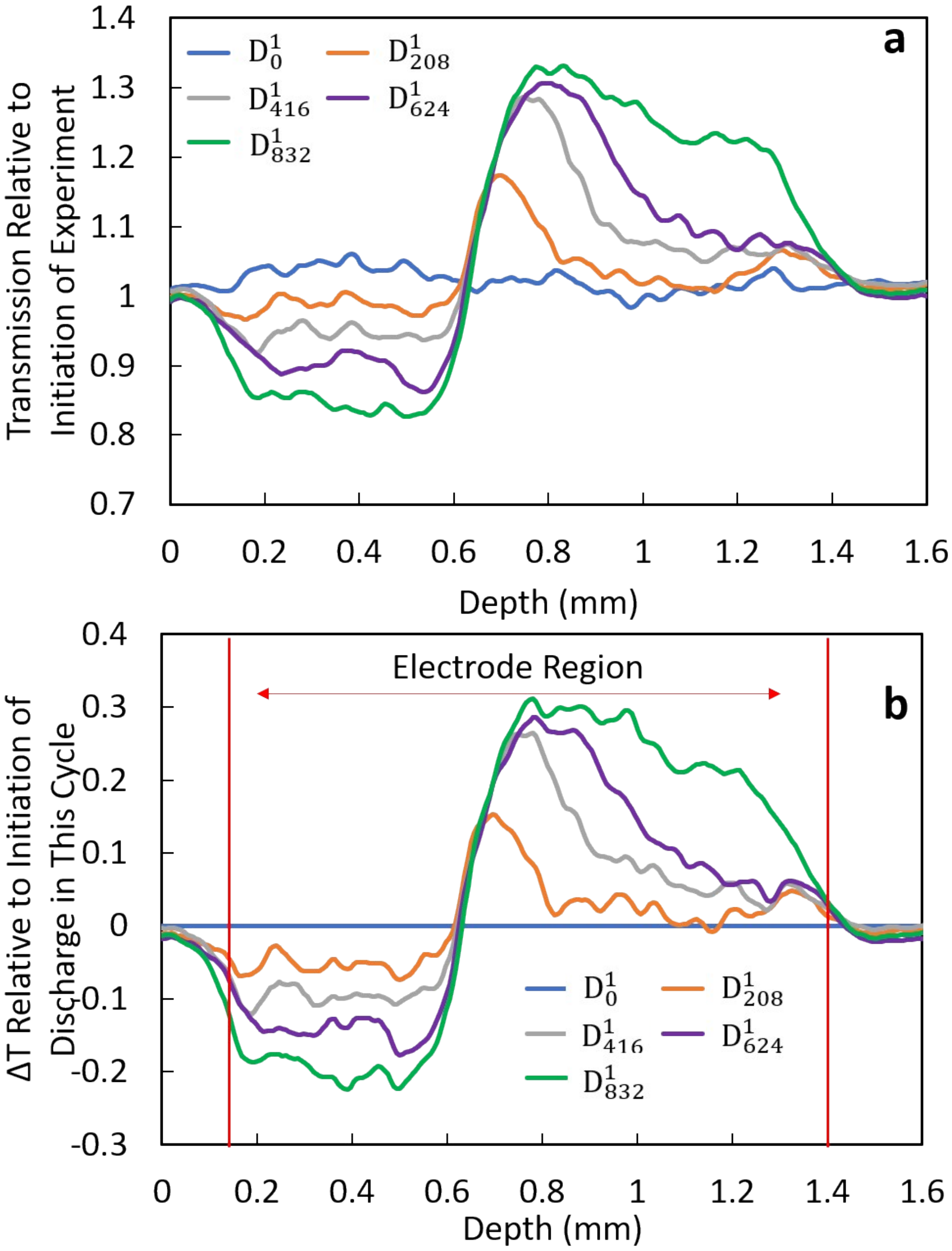

Fig. S9. (a) Relative transmission profiles of D^1 discharge process, where the transmission was relative to the initiation of the experiment. The depth of 0 corresponds to an arbitrary position slightly below LCO pellet in the stainless steel. (b) The same data as in (a) after subtracting the relative transmission observed at time D^1_0, which was the initiation of discharge in this cycle. Red vertical lines highlight the region of electrodes selected based on the method described above, and this region was rescaled from 0 mm for the final results shown in the main text in Fig. 4.

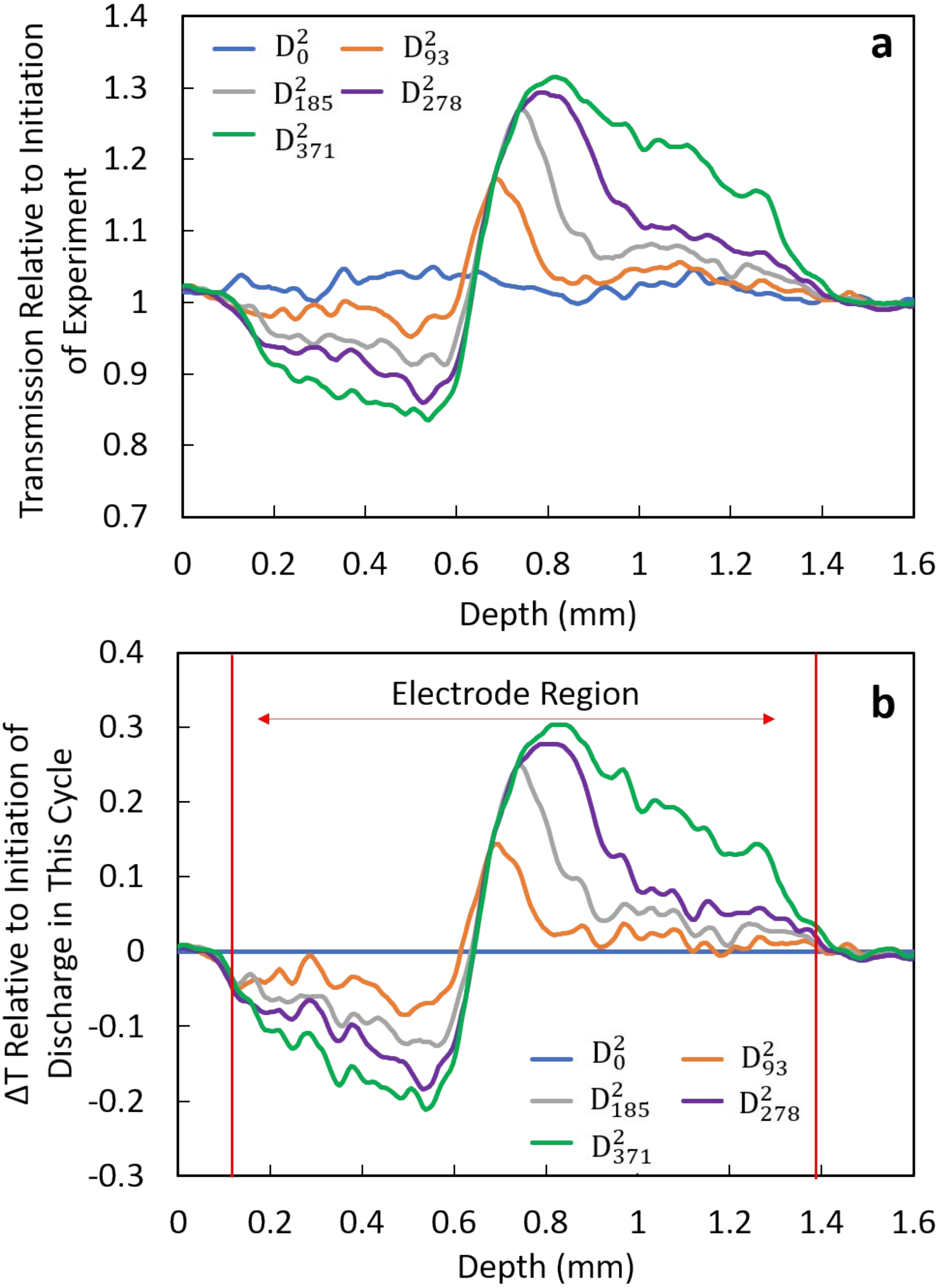

Fig. S10. (a) Relative transmission profiles of D^2 discharge process, where the transmission was relative to the initiation of the experiment. The depth of 0 corresponds to an arbitrary position slightly below LCO pellet in the stainless steel. (b) The same data as in (a) after subtracting the relative transmission observed at time D^2_0, which was the initiation of discharge in this cycle. Red vertical lines highlight the region of electrodes selected based on the method described above, and this region was rescaled from 0 mm for the final results shown in Fig. S14.

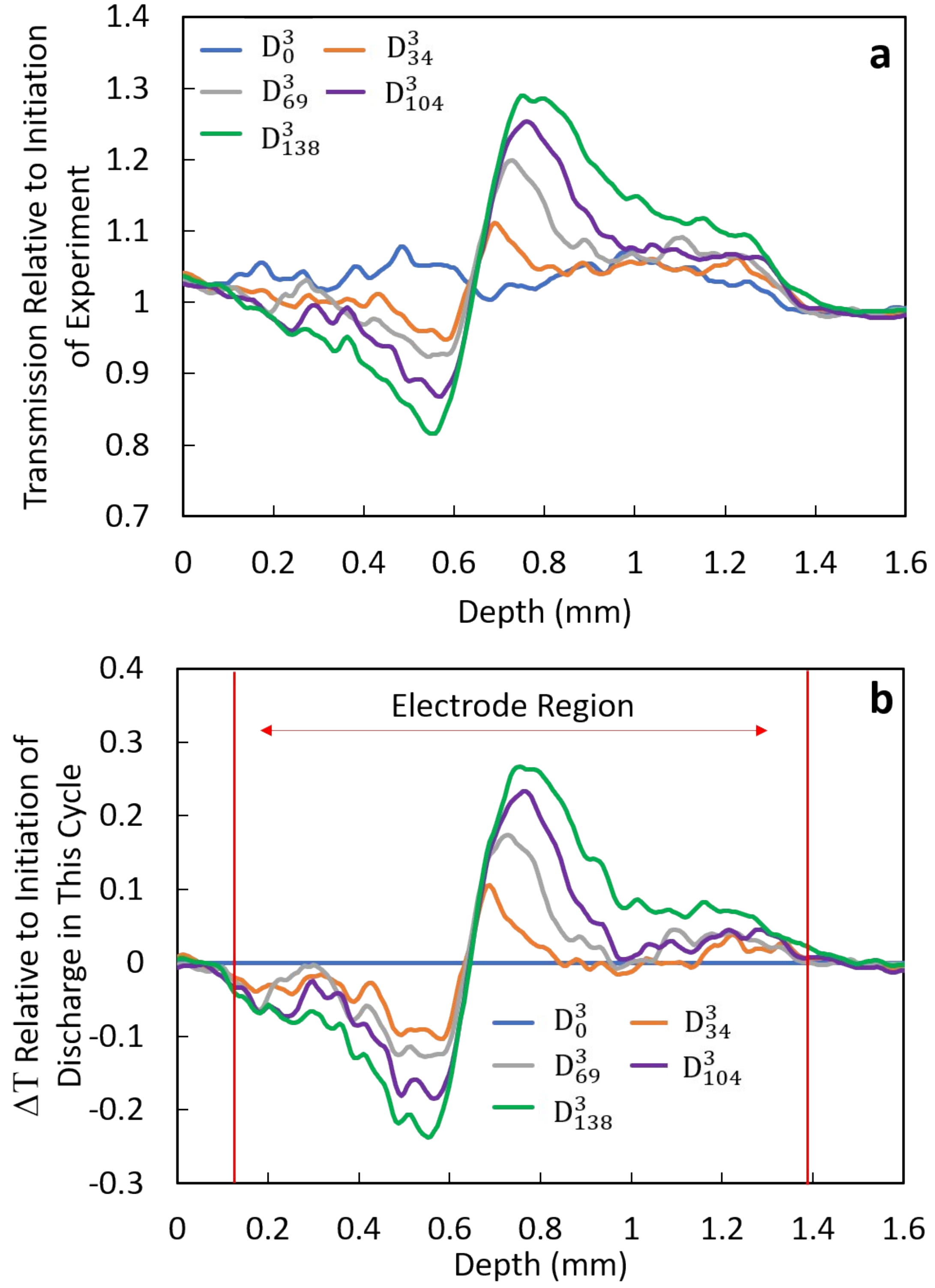

Fig. S11. (a) Relative transmission profiles of D^3 discharge process, where the transmission was relative to the initiation of the experiment. The depth of 0 corresponds to an arbitrary position slightly below LCO pellet in the stainless steel. (b) The same data as in (a) after subtracting the relative transmission observed at time D^3_0, which was the initiation of discharge in this cycle. Red vertical lines highlight the region of electrodes selected based on the method described above, and this region was rescaled from 0 mm for the final results shown in the main text in Fig. 5.

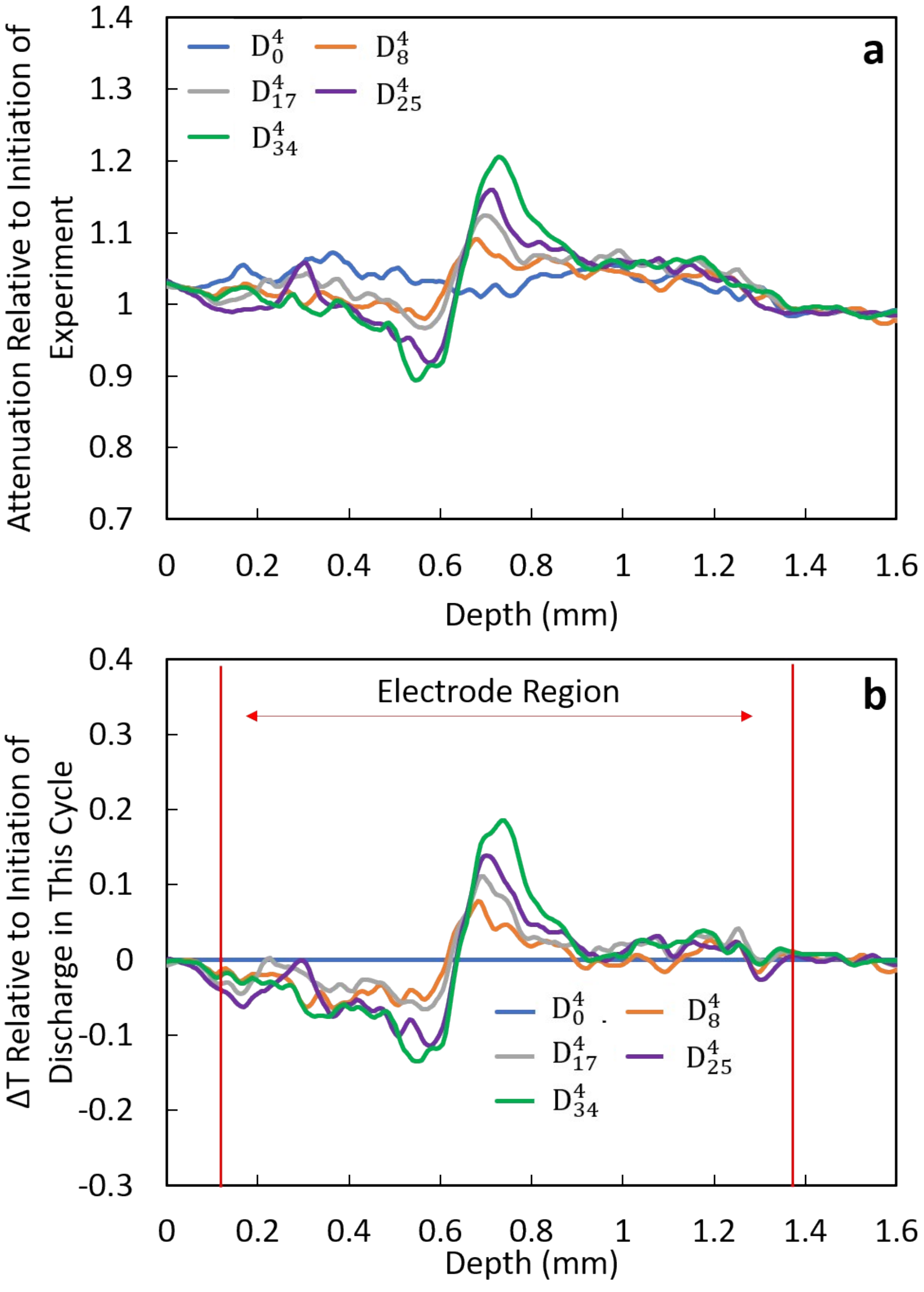

Fig. S12. (a) Relative transmission profiles of D^4 discharge process, where the transmission was relative to the initiation of the experiment. The depth of 0 corresponds to an arbitrary position slightly below LCO pellet in the stainless steel. (b) The same data as in (a) after subtracting the relative transmission observed at time D_0^4, which was the initiation of discharge in this cycle. Red vertical lines highlight the region of electrodes selected based on the method described above, and this region was rescaled from 0 mm for the final results shown in Fig. S15.

Selection of electrode region.

The line scan region was from a selected position below the LCO electrode to a selected position above the LTO electrode. Thus, the line scan profiles showed a depth longer than the total thickness of the real electrode region (Fig. S9, S10, S11, S12). To select the electrode region, the position of the bottom of the LCO, top of the LTO, and the separator must be located. To do this, a line scan was applied to the raw neutron imaging radiograph. The line scan region is shown in Fig. S13a. The image of Fig. S13a is the same one displayed in the main text Fig. 1b, but the contrast was adjusted to better display the inner structure of the coin cell. From Fig. S13a, the electrode region was clearly identified because the electrodes contain high concentrations of highly attenuating Li, and thus those regions were much darker than other regions in the coin cell. The transmission intensity profile is displayed in Fig. S13b. At the interface regions for different materials (e.g. stainless steel vs. LCO, LCO vs. LTO and LTO vs. stainless steel), there exists gradient regions. In this study, the midpoints of these gradient regions were chosen as the interface location. The bottom of LCO and the top of LTO pellet were thus located (Fig. S13b). The total thickness of the electrode region is 1.248 mm, which was 5 % greater than the experimentally measured combined thickness of the electrodes and separator, and this difference was attributed to image magnification and imperfect alignment of the cell. For the separator location, because the separator (25 μm) was much thinner than LCO (468 μm) and LTO (691 μm) pellets, a single line is shown in Fig. S13b instead of two lines representing the bottom and top of the separator. To confirm the selected locations for the electrode regions were consistent with the measured electrode dimension, comparison was made to the proportions of LCO and LTO electrodes. The physical measurements would result in LCO occupying 40.5 % of the total thickness and LTO occupying 59.5 % (assuming half the separator with each electrode). From the selected location in neutron imaging test, the LCO and LTO occupied 41.1 % and 58.9 % of total thickness, respectively, which was close to the physical measurements. Based on the three locations selected, the electrode region of the ΔTransmission profiles were chosen for each discharge process (Fig. S9b, S10b, S11b, S12b). The depth for the selected region with was rescaled to get the final ΔTransmission profiles showed in Fig. 4a, 5a, S14a, S15a.

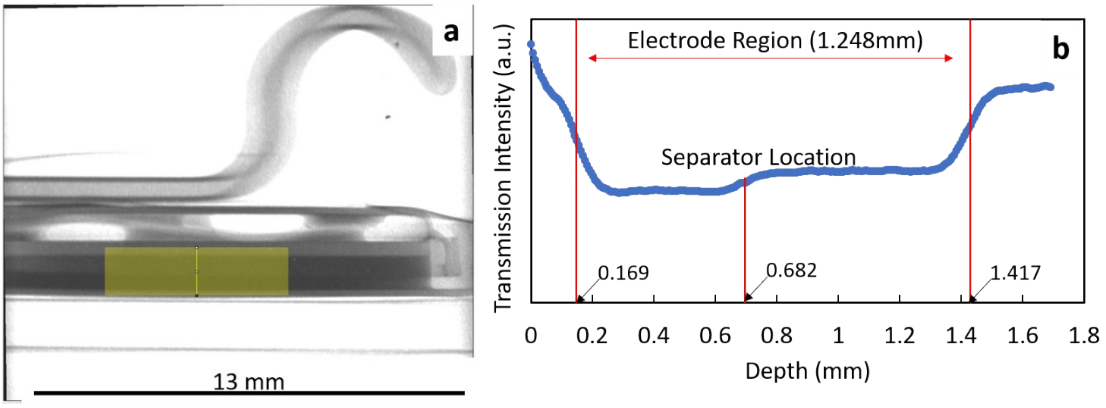

Fig. S13. (a) Neutron imaging radiograph. Image is the same as in main text Fig. 1b with contrast adjusted. (b) Line scan profiles of the yellow shaded region in (a), the scan direction was from bottom to top. Selected locations of LCO edge, LTO edge and separator are noted with red lines.

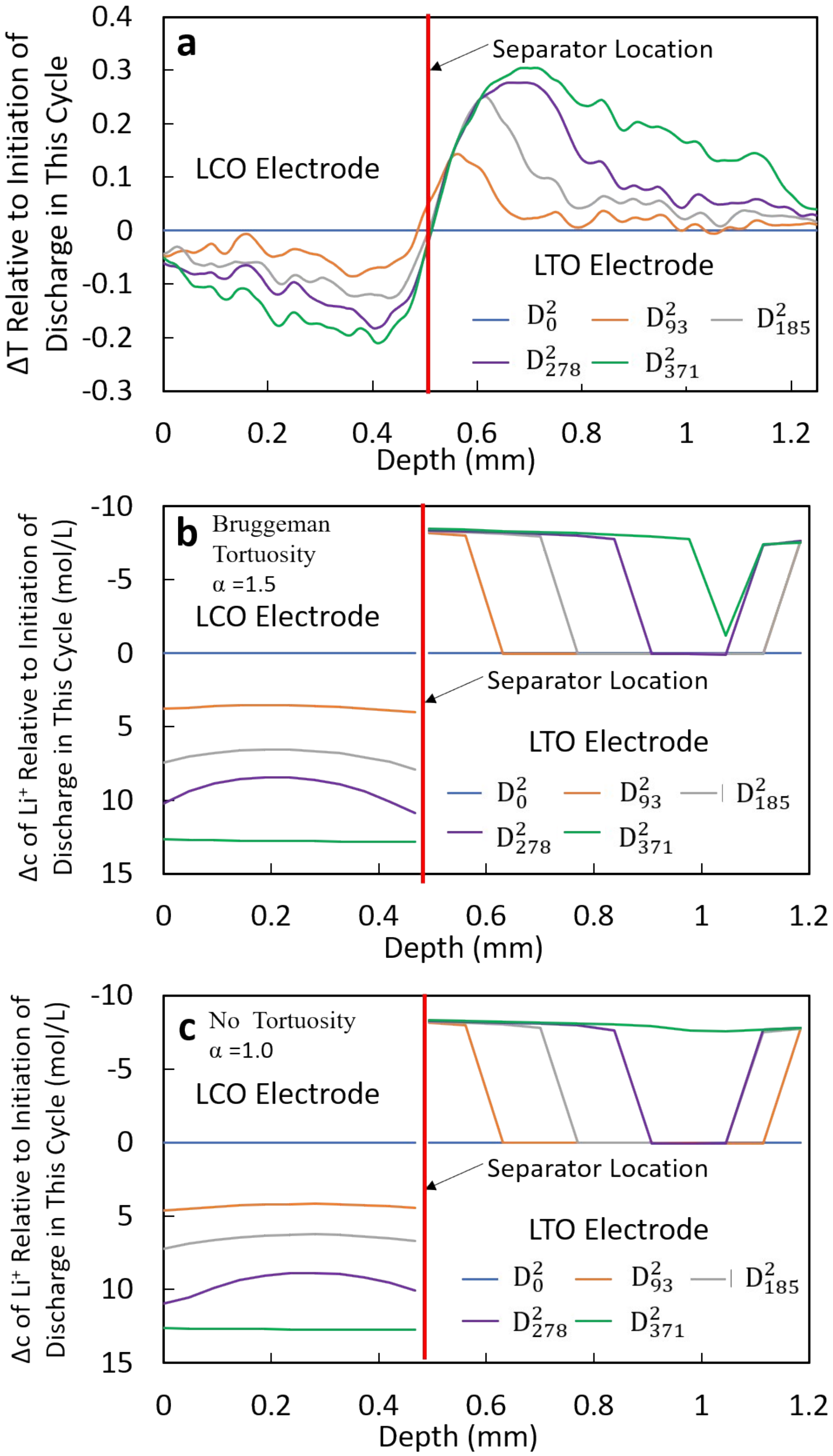

Fig. S14. Experimental and calculated results of D^2 discharge process. (a) ΔTransmission at different time relative to initiation of discharge in this cycle from neutron radiographs. (b) Calculated change in Li^+ concentration at different times relative to initiation of discharge in this cycle for α=1.5. (c) Calculated change in Li^+ concentration at different times relative to initiation of discharge in this cycle for α=1.0.

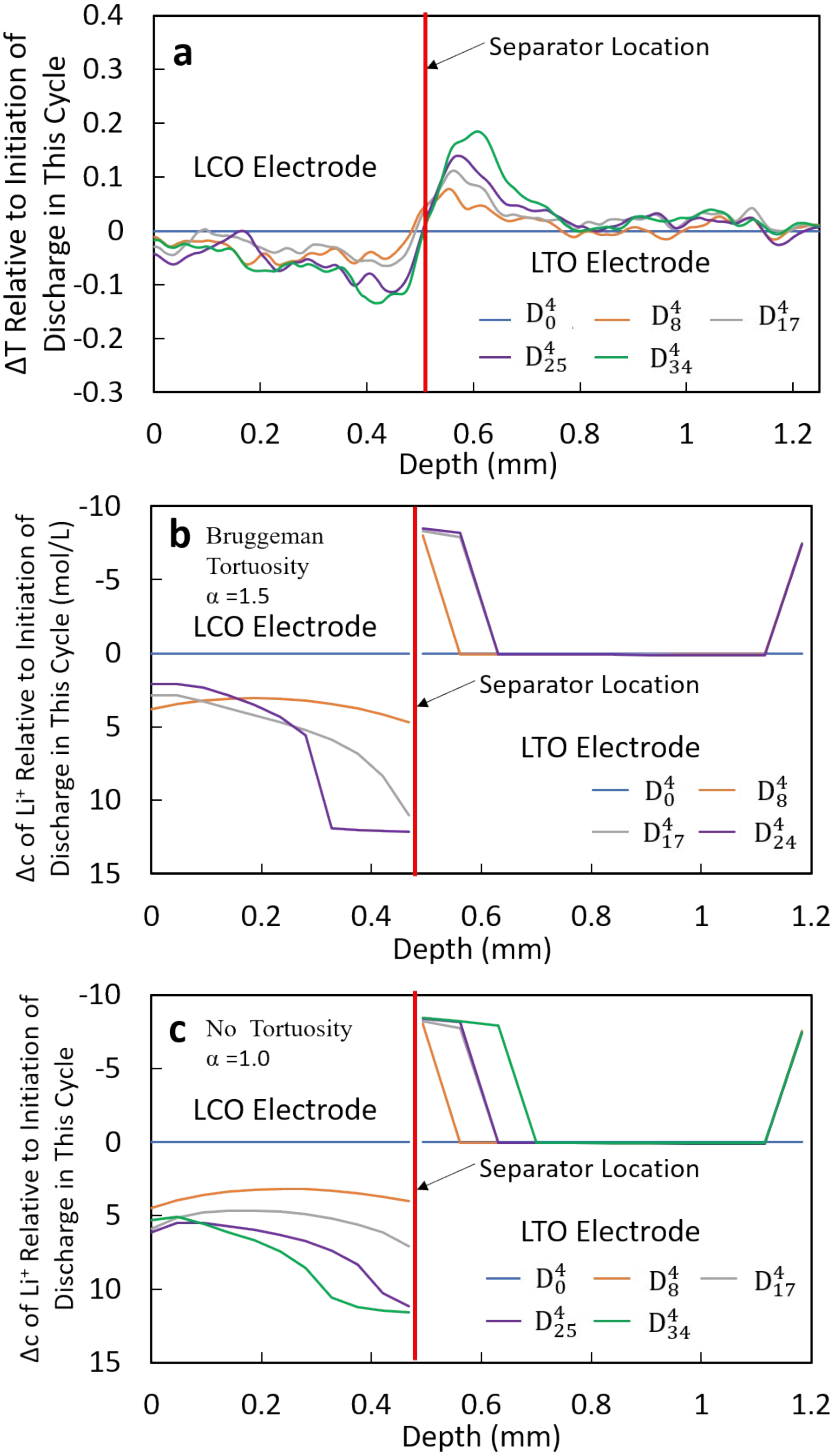

Fig. S15. Experimental and calculated results of D^4 discharge process. (a) ΔTransmission at different time relative to initiation of discharge in this cycle from neutron radiographs. (b) Calculated change in Li^+ concentration at different times relative to initiation of discharge in this cycle for α=1.5. (c) Calculated change in Li^+ concentration at different times relative to initiation of discharge in this cycle for α=1.0.

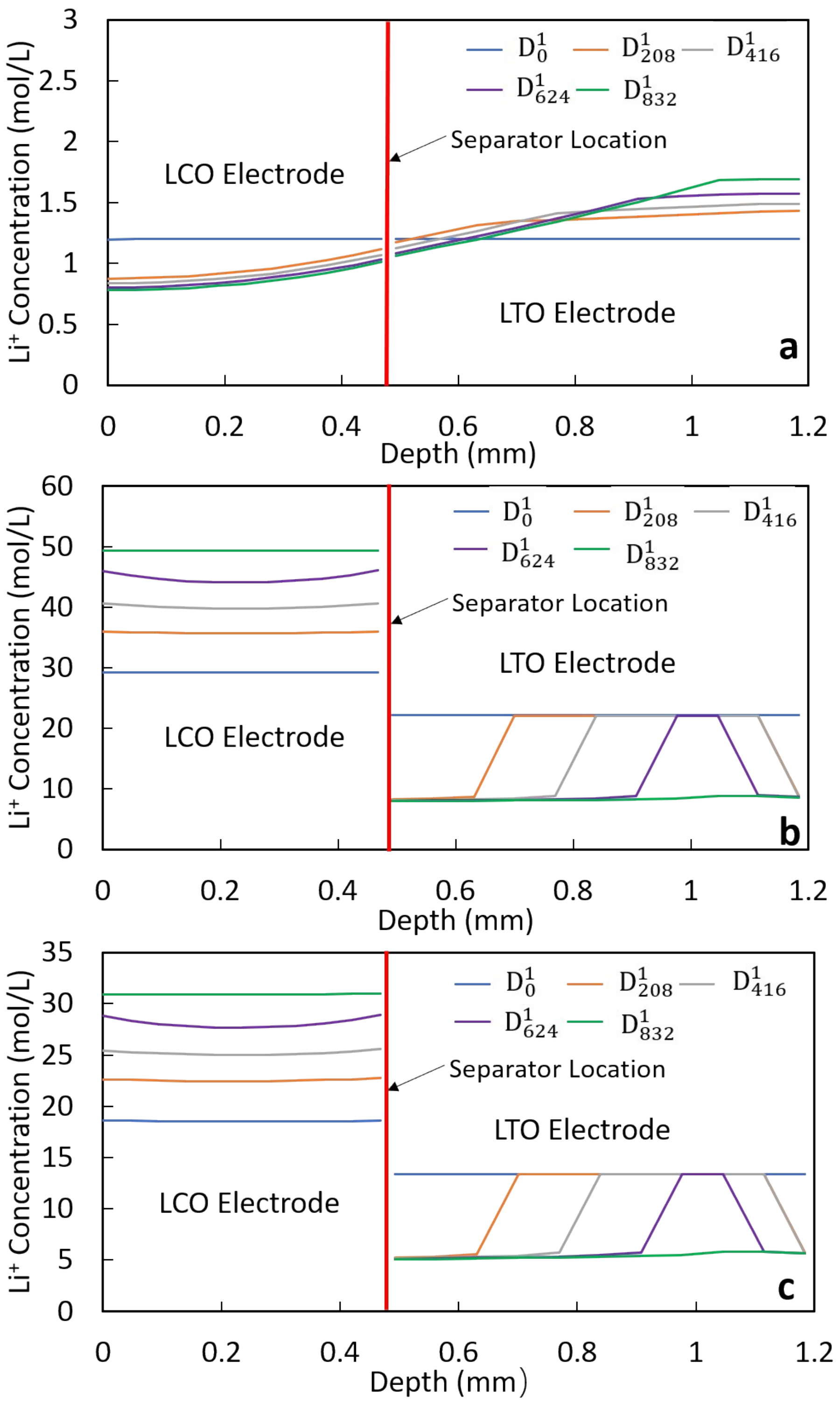

Fig. S16. Calculated Li^+ concentrations at different locations within both electrodes on a molar basis for D^1 process with Bruggeman tortuosity exponent $\alpha=1.5$. Concentrations are shown for the (a) liquid electrolyte phase, (b) solid active material phase, (c) and the sum of the total concentration. The subscript for each "D" corresponds to the time points in the discharge profile. Total concentration was calculated using the equation: $c_t=c_e\times\varepsilon+c_s\times(1-\varepsilon)$, where c_t is the total concentration, c_e is the concentration in electrolyte, c_s is the concentration in solid phase, ε is the electrode porosity.

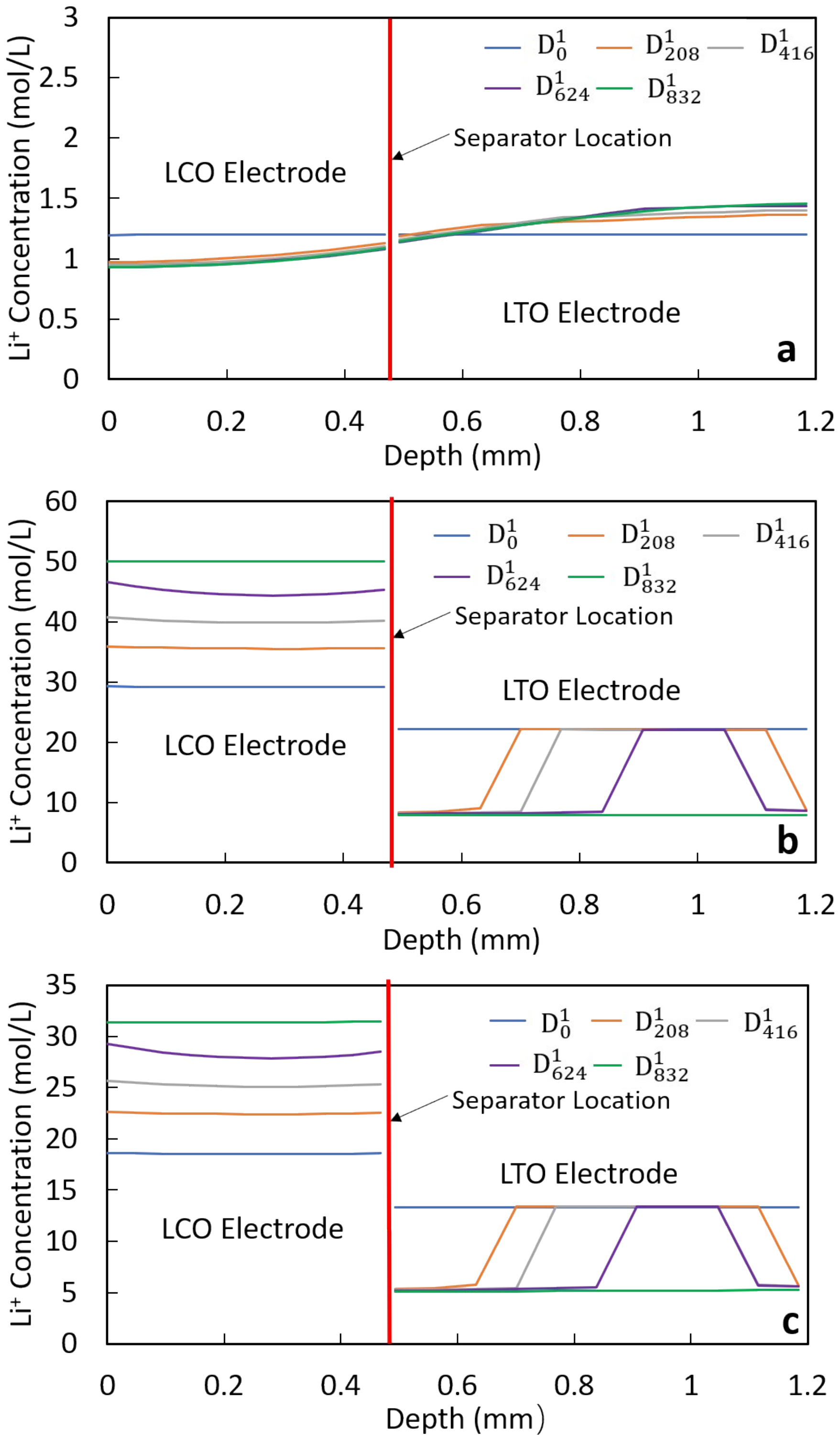

Fig. S17. Calculated Li$^+$ concentrations at different locations within both electrodes on a molar basis for D^1 process with no tortuosity (α=1.0). Concentrations are shown for the (a) liquid electrolyte phase, (b) solid active material phase, (c) and the sum of the total concentration. The subscript for each "D" corresponds to the time points in the discharge profile. Total concentration was calculated using the equation: $c_t=c_e\times\varepsilon+c_s\times(1-\varepsilon)$, where c_t is the total concentration, c_e is the concentration in electrolyte, c_s is the concentration in solid phase, ε is the porosity of the electrode.

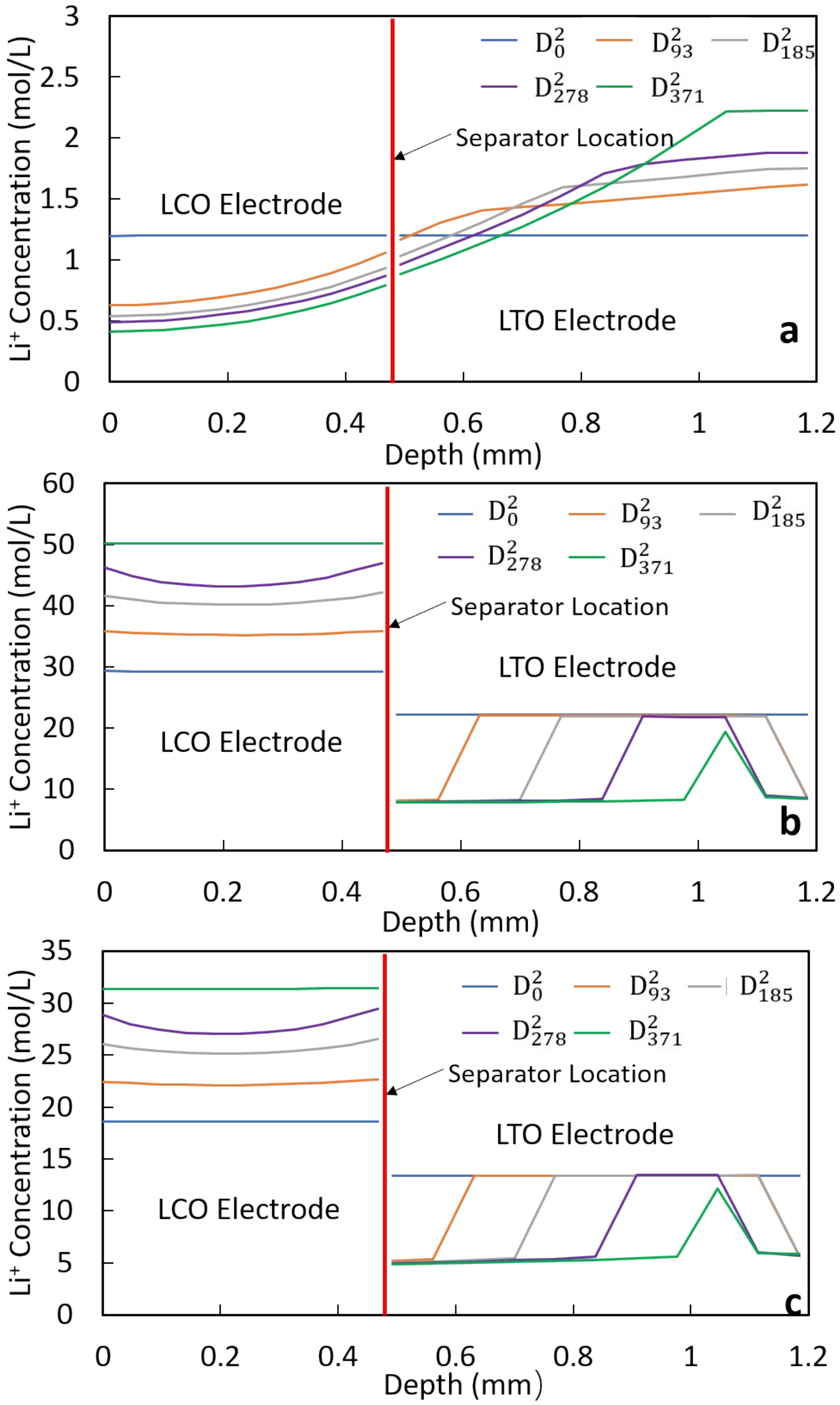

Fig. S18. Calculated Li^+ concentrations at different locations within both electrodes on a molar basis for D^2 process with Bruggeman tortuosity exponent $\alpha=1.5$. Concentrations are shown for the (a) liquid electrolyte phase, (b) solid active material phase, (c) and the sum of the total concentration. The subscript for each "D" corresponds to the time points in the discharge profile. Total concentration was calculated using the equation: $c_t=c_e\times\varepsilon+c_s\times(1-\varepsilon)$, where c_t is the total concentration, c_e is the concentration in electrolyte, c_s is the concentration in solid phase, ε is the electrode porosity.

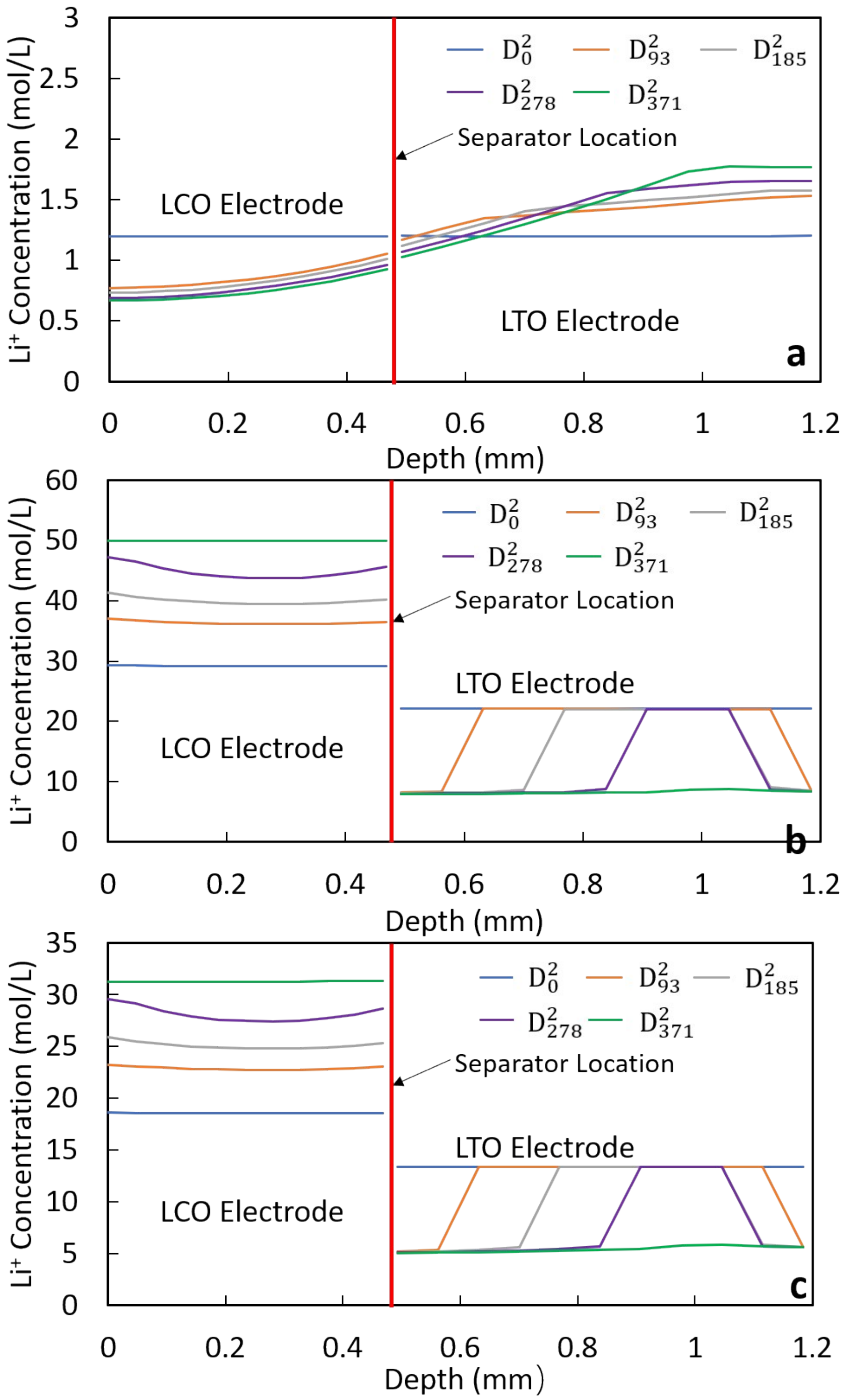

Fig. S19. Calculated Li$^+$ concentrations at different locations within both electrodes on a molar basis for D^2 process with no tortuosity (α=1.0). Concentrations are shown for the (a) liquid electrolyte phase, (b) solid active material phase, (c) and the sum of the total concentration. The subscript for each “D” corresponds to the time points in the discharge profile. Total concentration was calculated using the equation: $c_t=c_e\times\varepsilon+c_s\times(1-\varepsilon)$, where c_t is the total concentration, c_e is the concentration in electrolyte, c_s is the concentration in solid phase, ε is the porosity of the electrode.

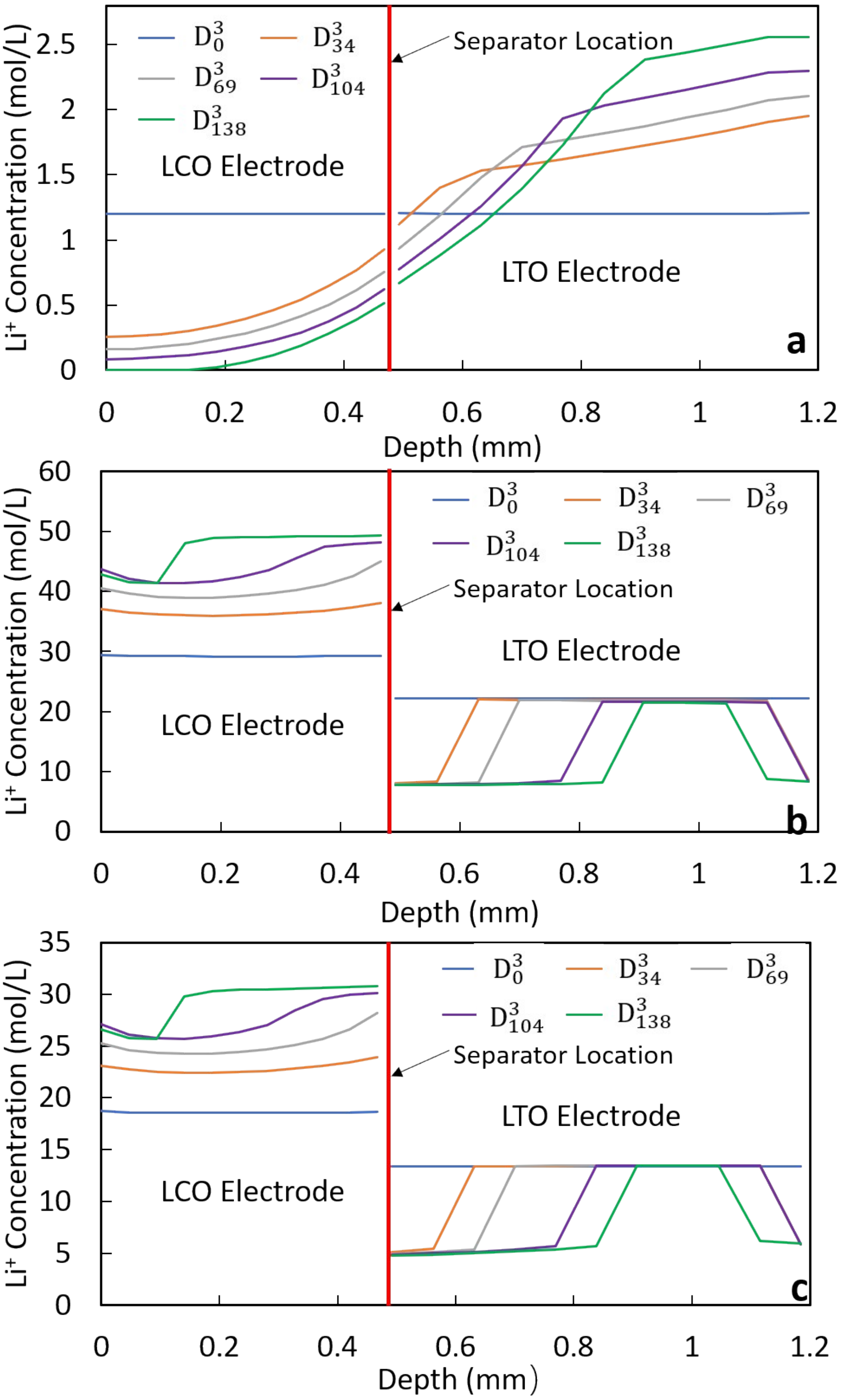

Fig. S20. Calculated Li$^+$ concentrations at different locations within both electrodes on a molar basis for D^3 process with Bruggeman tortuosity exponent α=1.5. Concentrations are shown for the (a) liquid electrolyte phase, (b) solid active material phase, (c) and the sum of the total concentration. The subscript for each "D" corresponds to the time points in the discharge profile. Total concentration was calculated using the equation: $c_t = c_e \times \varepsilon + c_s \times (1-\varepsilon)$, where c_t is the total concentration, c_e is the concentration in electrolyte, c_s is the concentration in solid phase, ε is the electrode porosity.

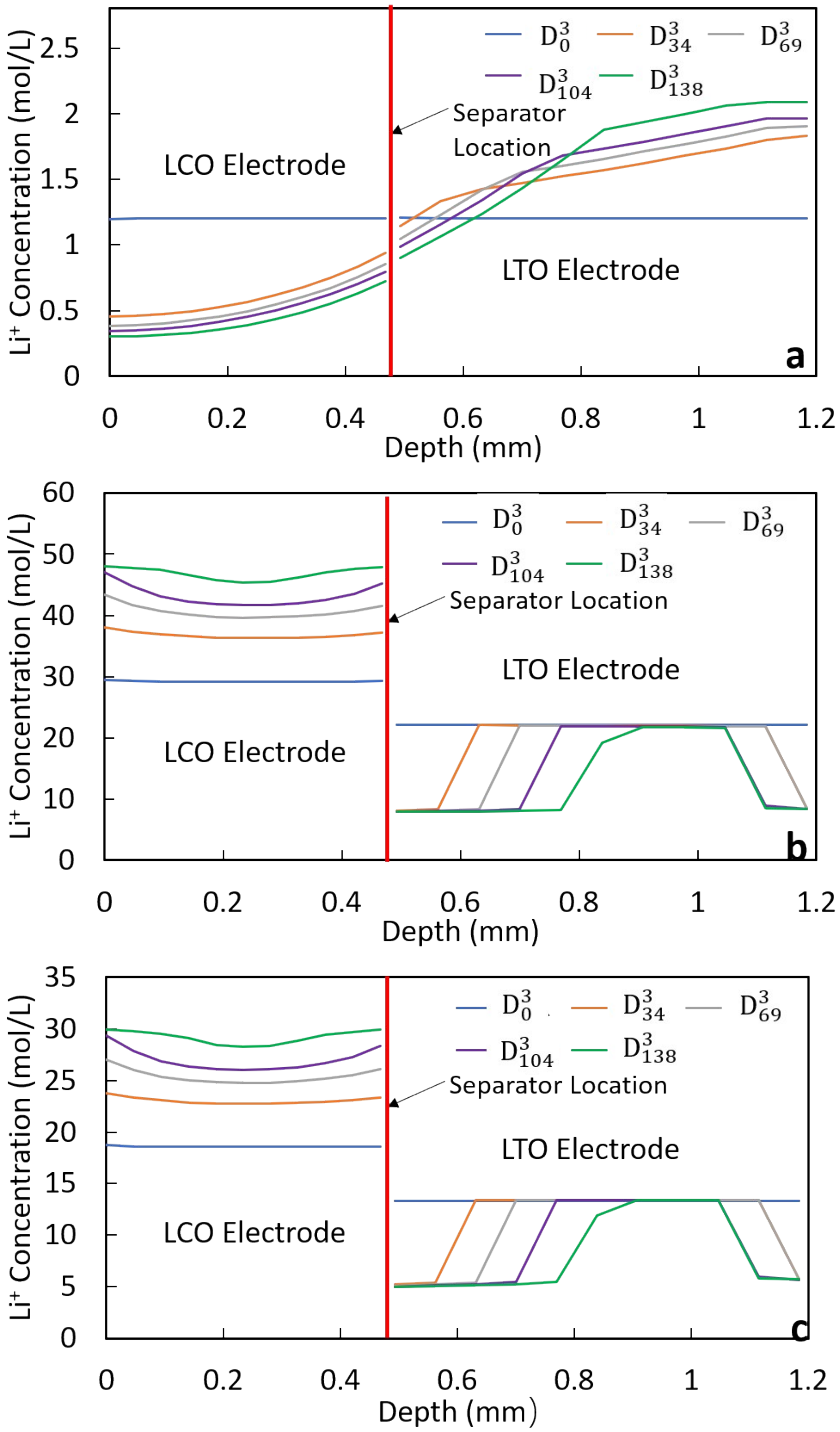

Fig. S21. Calculated Li^+ concentrations at different locations within both electrodes on a molar basis for D^3 process with no tortuosity (α=1.0). Concentrations are shown for the (a) liquid electrolyte phase, (b) solid active material phase, (c) and the sum of the total concentration. The subscript for each "D" corresponds to the time points in the discharge profile. Total concentration was calculated using the equation: $c_t=c_e\times\varepsilon+c_s\times(1-\varepsilon)$, where c_t is the total concentration, c_e is the concentration in electrolyte, c_s is the concentration in solid phase, ε is the porosity of the electrode.

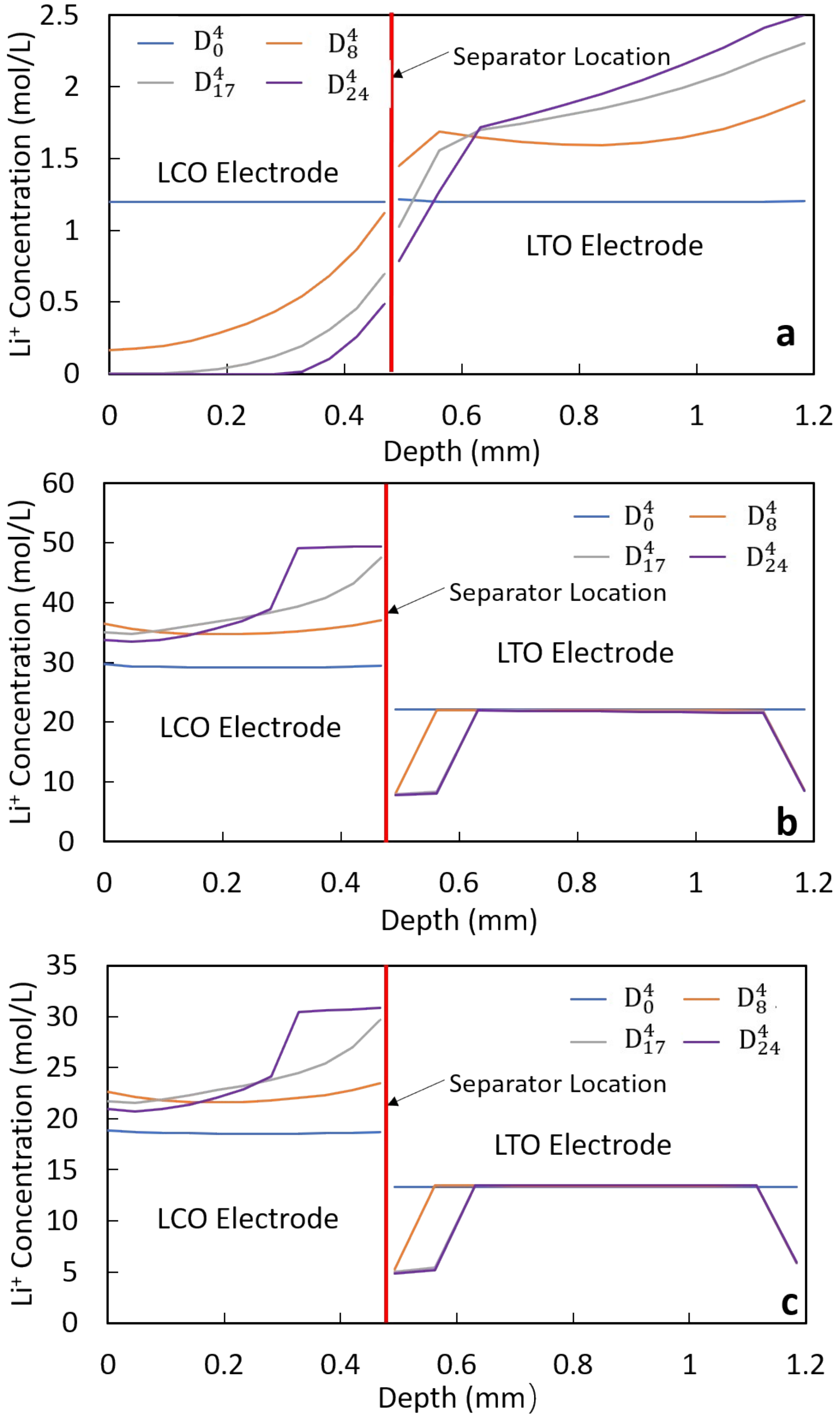

Fig. S22. Calculated Li^+ concentrations at different locations within both electrodes on a molar basis for D^4 process with Bruggeman tortuosity exponent $\alpha=1.5$. Concentrations are shown for the (a) liquid electrolyte phase, (b) solid active material phase, (c) and the sum of the total concentration. The subscript for each "D" corresponds to the time points in the discharge profile. Total concentration was calculated using the equation: $c_t=c_e\times\varepsilon+c_s\times(1-\varepsilon)$, where c_t is the total concentration, c_e is the concentration in electrolyte, c_s is the concentration in solid phase, ε is the electrode porosity.

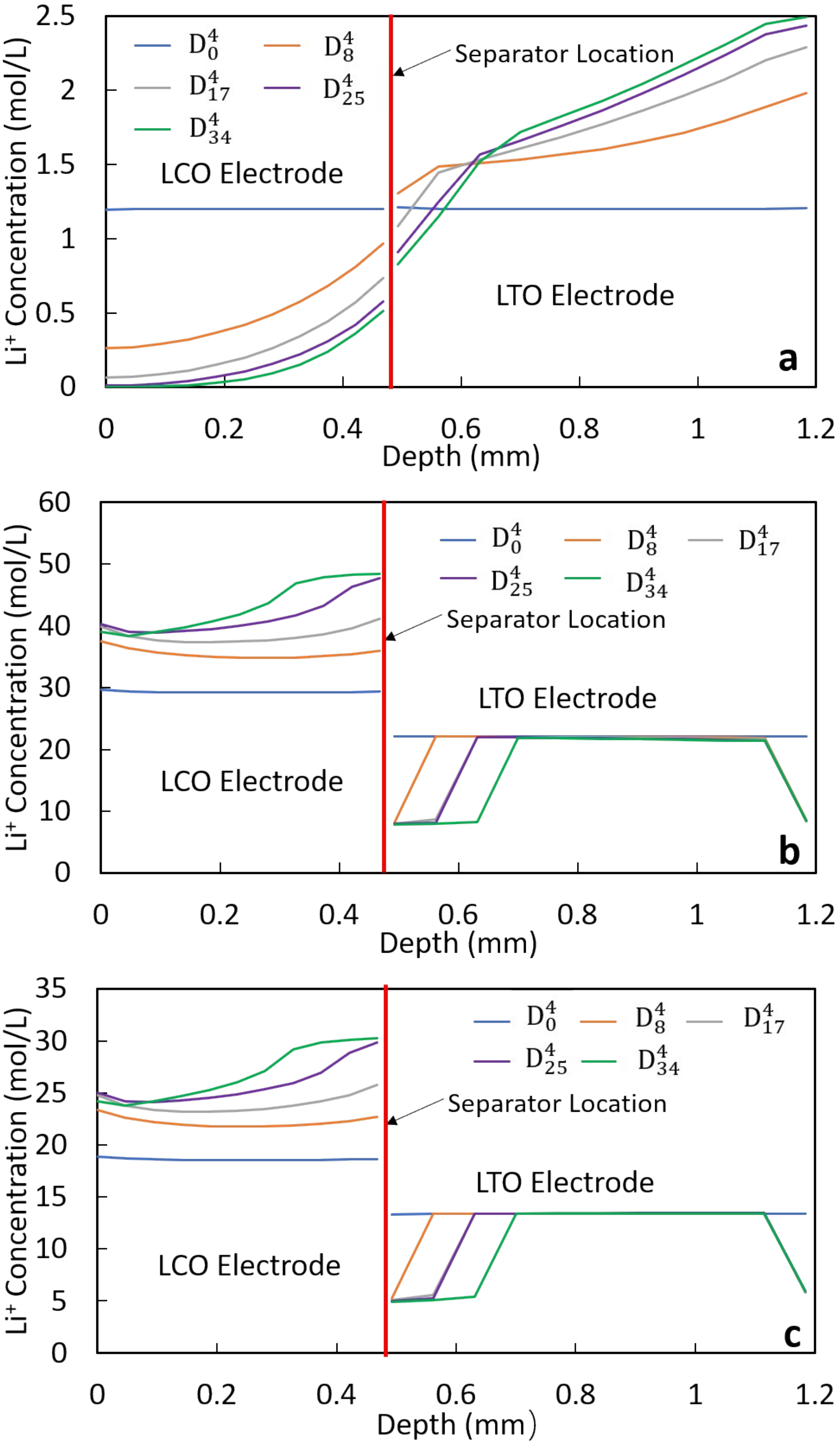

Fig. S23. Calculated Li⁺ concentrations at different locations within both electrodes on a molar basis for D^4 process with no tortuosity (α=1.0). Concentrations are shown for the (a) liquid electrolyte phase, (b) solid active material phase, (c) and the sum of the total concentration. The subscript for each "D" corresponds to the time points in the discharge profile. Total concentration was calculated using the equation: $c_t=c_e\times\varepsilon+c_s\times(1-\varepsilon)$, where c_t is the total concentration, c_e is the concentration in electrolyte, c_s is the concentration in solid phase, ε is the porosity of the electrode.

References.

1 I. V. Thorat, D. E. Stephenson, N. A. Zacharias, K. Zaghib, J. N. Harb and D. R. Wheeler, *J. Power Sources*, 2009, **188**, 592-600.

2 M. Ménétrier, I. Saadoune, S. Levasseur and C. Delmas, *J. Mater. Chem.*, 1999, **9**, 1135–1140.

3 D. Young, A. Ransil, R. Amin, Z. Li and Y. M. Chiang, *Adv. Energy Mater*, 2013, **3**, 1125–1129..

4 P. Albertus and J. Newman, Introduction to dualfoil 5.0, University of California Berkeley, Berkeley, CA, Tech. Rep. 2007.

5 C. Capiglia, Y. Saito, H. Kageyama, P. Mustarelli, T. Iwamoto, T. Tabuchi and H. Tukamoto, *J. Power Sources*, 1999, **81**, 859-862.

6 C. M. Doyle, PhD Thesis, Lawrence Berkeley Laboratory, 1995.